Check for updates

JGR Oceans

RESEARCH ARTICLE
10.1029/2020JC016528

Shelf Seas Baroclinic Energy Loss: Pycnocline Mixing and Bottom Boundary Layer Dissipation

Mark E. Inall[1], Matthew Toberman[1], Jeff A. Polton[2], Matthew R. Palmer[2], J. A. Mattias Green[3], and Tom P. Rippeth[3]

[1]Scottish Association for Marine Science, Dunstaffnage Marine Laboratory, Oban, UK, [2]National Oceanography Centre, Liverpool, UK, [3]University of Bangor, Wales, UK

Key Points:

- Pycnocline dissipation is locally higher than internal tide conversion at low conversion rates, but lower at high conversion
- Overall, pycnocline dissipation alone accounts for ~25% of conversion, and requires bottom boundary layer dissipation to achieve balance
- Local diapycnal mixing does not increase linearly with tidal conversion, but rather with a one-third power law

Correspondence to:
M. E. Inall,
mark.inall@sams.ac.uk

Citation:
Inall, M. E., Toberman, M., Polton, J. A., Palmer, M. R., Green, J. A. M., & Rippeth, T. P. (2021). Shelf seas baroclinic energy loss: Pycnocline mixing and bottom boundary layer dissipation. *Journal of Geophysical Research: Oceans*, *126*, e2020JC016528. https://doi.org/10.1029/2020JC016528

Received 19 JUN 2020
Accepted 23 JUL 2021

Abstract Observations of turbulent kinetic energy dissipation rate (ϵ) from a range of historical shelf seas data sets are viewed from the perspective of their forcing and dissipation mechanisms: barotropic to baroclinic tidal energy conversion, and pycnocline and bottom boundary layer (BBL) dissipation. The observations are placed in their geographical context using a high resolution numerical model (NEMO AMM60) in order to compute relevant maps of the forcing (conversion). We analyze, in total, 18 shear microstructure surveys undertaken over a 17 year period from 1996 to 2013 on the North West European shelf, consisting of 3,717 vertical profiles of shear microstructure: 2,013 from free falling profilers and 1,704 from underwater gliders. A robust positive relationship is found between model-derived barotropic to baroclinic conversion, and observed pycnocline integrated ϵ. A fitted power law relationship of approximately one-third is found, giving a simple new parameterization. We discuss reasons for this apparent power law and where the "missing" dissipation may be occurring. We conclude that internal wave related dissipation in the bottom boundary layer provides a robust explanation and is consistent with a commonly used fine-scale pycnocline dissipation parameterization.

Plain Language Summary Waves on the surface of the ocean are clear for all to see. Beneath the ocean's surface exists a type of wave called internal waves. One reason these waves exist is because the motion of the ocean's tides pushes deeper, cooler water up and down sloping regions of the seabed, such as the edge of the continental shelf. Thus, shelf seas are particularly energetic places for internal waves driven by the tide (often called internal tides). Internal tides can travel long distances and lose energy by "breaking" along the interface between deeper cool layers, and warmer surface layers. Wave breaking causes mixing up of cold, nutrient rich waters which play an important role in feeding the summertime shelf seas ecosystems. But, it is not just wave breaking that takes energy from internal tides. In this article, we examine the way in which internal tides interact with the sea bed of the shelf seas, and show that it is friction at the sea bed, rather than wave breaking, that takes most of the energy from internal tide waves. Perhaps counterintuitively, as internal tides get larger, this sea bed effect increases far more rapidly than does wave breaking.

1. Introduction

Continental shelf seas occupy ~7% of the global ocean surface area yet are disproportionately influential in the Earth's system as a critical interface linking the marine, atmospheric, and terrestrial components (Rippeth, 2005). They provide a sink for ~70% of tidal energy dissipation (Munk & Wunsch, 1998). They also play a significant role in the global cycling of carbon by the oceans (Sharples et al., 2019), estimated to account for between 10 and 30% of total marine primary production, and as a consequence a significant proportion of carbon burial (Bauer et al., 2013).

The first order paradigm for shelf sea mechanical energy balance has largely focused on mixing at the upper and lower boundaries, due to wind stress and barotropic tidal currents, respectively (Simpson & Hunter, 1974). However, within regions of seasonal stratification and linked to the presence of the steep shelf break the internal tide has been shown to make a larger contribution to diapycnal mixing than the barotropic tide (Rippeth et al., 2005).

In contrast to the deep ocean, the seasonal shelf sea pycnocline is observed to exist predominantly in a state of marginal stability with respect to a fine scale (of order several meters) Richardson Number ($Ri \sim 1$)

© 2021. The Authors.
This is an open access article under the terms of the Creative Commons Attribution License, which permits use, distribution and reproduction in any medium, provided the original work is properly cited.

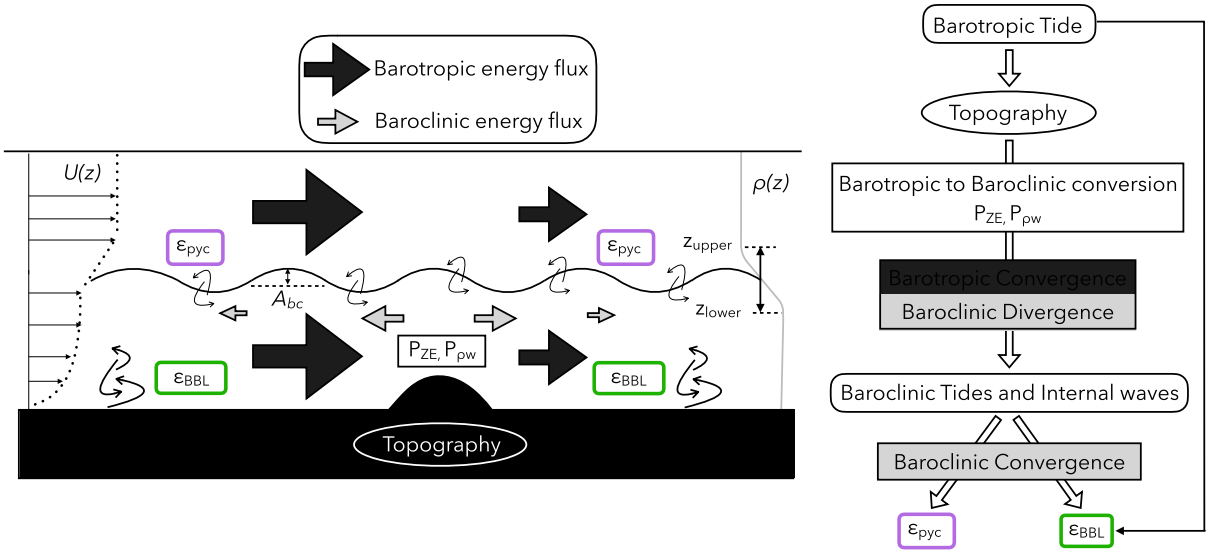

Figure 1. Schematic describing the conversion of barotropic tidal energy to baroclinic energy, and the dual fates of that energy in shelf seas. Barotropic tidal energy is converted to baroclinic energy over topography, resulting in a convergence of barotropic, and divergence of baroclinic energy. Internal waves (of amplitude A_{bc}) radiate away from this generation site. Baroclinic energy is dissipated and thus converges in two ways. (a) Within the pycnocline, ϵ_{pyc}. (b) In the bottom boundary layer turbulence ϵ_{bbl} (which is also fueled directly from bottom friction acting on the barotropic tide). An idealized profile of shelf sea vertical density structure is shown demonstrating the pycnocline selection criteria described in the text. An idealized shelf sea velocity profile, $U(z)$ is also shown.

(MacKinnon & Gregg, 2003; Palmer et al., 2008; Rippeth, 2005; van Haren et al., 1999). Higher stratification (i.e., increased stability) leads to greater conversion of barotropic to baroclinic kinetic energy, increasing baroclinic shear driven mixing, which dissipates and mixes, in turn reducing stratification (stability) and thus returning the system to a state of marginal stability. The existence of the marginally stable state mediates the shoreward energy flux associated with the internal tide. The precise relationship between conversion and dissipation and mixing, however, remains unclear.

Overall, the rate of diapycnal mixing is a critical control on the vertical fluxes of nutrients, heat and salt as well as modifying the vertical location of the pycnocline itself, thus demonstrating the need to accurately parameterize mixing processes within shelf sea models.

In this article, we explore in more detail the influence of bed friction on pycnocline mixing (see Figure 1), speculated about briefly in previous studies (Inall & Rippeth, 2002; Inall et al., 2000; MacKinnon & Gregg, 2003). While it has been shown that dissipation in the bottom boundary may not exert a direct control on pycnocline mixing (Rippeth, 2005), an indirect control is investigated here by considering separately the influence of internal friction and boundary friction on the internal wave energy flux divergence.

Currently, many shelf sea models include a turbulence closure vertical mixing scheme (e.g., Holt & Umlauf, 2008). However, when profiles of turbulent kinetic energy dissipation rate predicted using 1D versions of the closure schemes are compared with observations they have failed to correctly reproduce the dissipation rates within the pycnocline. Without the inclusion of artificial adjustments, including high levels of background diffusion (Simpson et al., 1996), the closure schemes are inadequate. Some improvements have been made in reproducing shelf seas mixing with high resolution numerical models, through the development and implementation of a hierarchy of second moment turbulence closure schemes (Holt & Umlauf, 2008). In order to simulate internal mixing, these schemes apply various different stability functions derived from the ratio of the local buoyancy frequency to local velocity shear, to relate prognostic turbulent length and time scale terms to the mean flow characteristics. However, without *ad hoc* enhancements these second moment turbulence closure schemes generally do not generate enough mixing across the pycnocline within seasonally stratified shelf seas (Holt & Umlauf, 2008; Rippeth, 2005). This has been taken to imply that the current models do not represent certain key processes which generate shear at the pycnocline; particularly internal waves or wind-driven inertial oscillations (Rippeth et al., 2005). Partly in order to resolve this issue, and also to improve model stability, an *ad hoc* and high level of background diffusion is

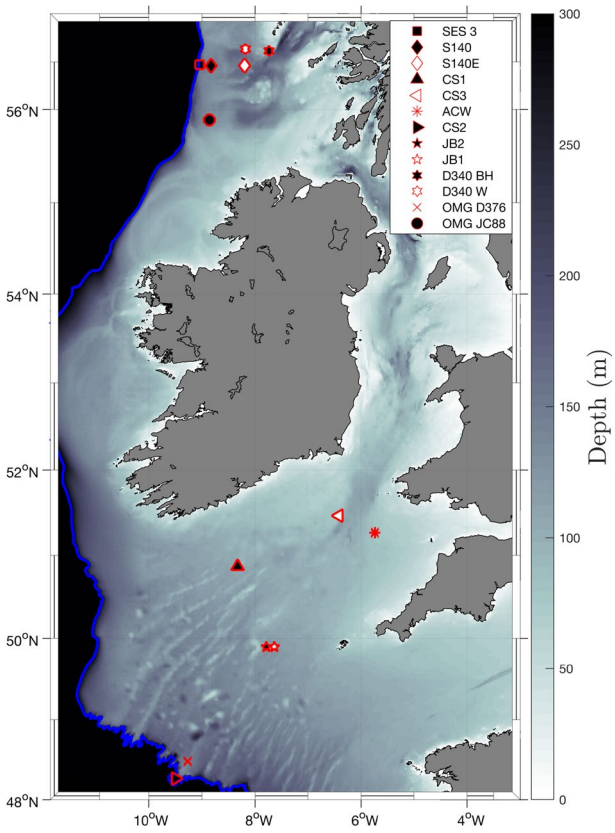

Figure 2. Locations of microstructure observational campaigns as detailed in Table 1. Blue line shows 300 m depth contour.

often applied throughout model domains (Jochum, 2009), justified on the dual grounds of tuning to observations and of numerical stability. This approach can lead to an improvement in reproducing observed levels of mixing in some areas, but often fails to do so within stratified regions (Luneva et al., 2019). Uniformly applied diffusive mixing also fails, by definition, to represent the significant temporal and spatial variability known to exist within ocean turbulence (Moum & Rippeth, 2009). Indeed, a recent study (Luneva et al., 2019), which examined a number of commonly used numerical mixing schemes adapted to overcome missing sub-grid scale dynamics in a 7 km resolution hydrodynamic model (the NEMO AMM7 model), demonstrated that many commonly used enhanced second order mixing schemes lead to an overly diffusive water column when implemented in the latest generation of shelf seas hydrodynamic models.

These model limitations have hampered our ability to make meaningful comparisons between modeled internal wavefield energetics and a shelf-wide observational database of turbulent kinetic energy dissipation estimates. However, recent enhancements of the NEMO shelf model to 1.8 km horizontal resolution (AMM60) have resulted in an increased ability to systematically permit internal tide generation and propagation (Guihou et al., 2018). AMM60 successfully simulated internal tides with realistic spectral energy at diurnal, inertial, semi-diurnal and quarter-diurnal bands, and tidally induced pycnocline displacements were diagnosed to vary with the spring neap cycle. A detailed study of vertical mixing and dissipative processes within AMM60 is yet to be undertaken, and is not the purpose here. Rather, our aim is to take the successes of AMM60 in reproducing internal tides (Guihou et al., 2018) and explore the relationship between model-based tidal conversion estimates and observations of turbulent kinetic energy dissipation within the pycnocline. Our exploration is primarily motivated by a small number of studies which noted the potentially significant role of lower boundary friction as the dominant energy sink from internal waves in shallow seas (Inall & Rippeth, 2002; Inall et al., 2000; MacKinnon & Gregg, 2003). These previous observations suggest that the energy available for pycnocline mixing may be inextricably linked to energy loss in the lower boundary layer.

Our aim is achieved by collating and reanalyzing a large historical collection of microstructure observations of turbulent kinetic energy dissipation data (hereafter ϵ), all obtained on the relatively wide and flat North West European continental shelf (Figure 2); an area of large tidal conversion (Baines, 1982; Egbert & Ray, 2001; Nycander, 2005), large amplitude internal tides, and enhanced pycnocline mixing (Inall et al., 2001, 2011; Palmer et al., 2008; Rippeth & Inall, 2002; Sharples et al., 2007; Sherwin, 1988). Historically, microstructure derived observations of ϵ have often been targeted toward regions known to exhibit specific processes, such as internal waves (Moum et al., 2003), gravity currents (Kilcher & Nash, 2010) or indeed boundary layer processes (Rippeth et al., 2001; Simpson et al., 1996). This is due, at least in part, to an *a priori* expectation that observing the turbulence is key to understanding the dynamics of these processes, and how they are coupled to the larger scale mean flow. Microstructure surveys spanning larger horizontal scales are rare (Polzin et al., 1997; Vic et al., 2018, 2019), although the advent of microstructure equipped ocean gliders is beginning to address this limitation by extending both the duration and extent over which shear microstructure can be observed (Fer et al., 2014; Lucas et al., 2019; Palmer et al., 2015; Schultze et al., 2017). Due to the temporal and spatial restrictions related to microstructure observations, previous studies that investigate how microstructure derived turbulence varied across large spatial areas have consisted of a synthesis of previous observational campaigns, for example, (St. Laurent & Simmons, 2006; Waterhouse et al., 2014). The studies of St. Laurent and Simmons (2006) and Waterhouse et al. (2014) both investigated global patterns of turbulent mixing using the pre-existing databases of ϵ measurements available at the time. Both of these studies focused on the deep ocean, purposefully excluding shelf sea regions. Here we draw together 18 shelf seas microstructure data sets, comprising in a total of more than 3,700 profiles

from the Northwest European shelf (Figure 2). This presents the first opportunity to investigate spatial patterns of turbulence across a wide shelf sea environment.

These 18 observational data sets from the Northwest European shelf are compared with two separate formulations of internal tide forcing computed using output from a 1.8 km resolution numerical model (Guihou et al., 2018). We view the resulting relationship through the lens of a commonly used pycnocline parameterization scheme in order to explore the relationship between internal and external (lower boundary) frictional energy losses. In all that follows, we stress the focus on spatial variability and energetic relationships averaged over time (tidal cycle) applicable to the stratified summer period.

2. Numerical Formulation of Baroclinic Forcing Terms

To place the 18 ϵ data sets within a common dynamical framework we use output from a three-dimensional hydrodynamic ocean simulation with a 1.8 km (1 / 60°) horizontal resolution, using the Nucleus for European Modeling of the Ocean (NEMO) framework based on v3.6. This NEMO configuration, AMM60, has 51 terrain following (s-sigma) vertical levels, is forced by ERA-Interim atmospheric forcing, TPXO7.2 tides and a North Atlantic NEMO configuration at the lateral boundaries. For details, see Guihou et al. (2018). AMM60 was the developmental precursor to FOAM AMM15, which in 2021 is the current UK Met Office operational model for the NW European Shelf Seas (Graham et al., 2018; Tonani et al., 2019).

Output from the AMM60 model (Guihou et al., 2018) is used to quantify the barotropic tidal forcing of the internal wavefield across the full region covering all microstructure surveys. Two linear forms of a barotropic to baroclinic tidal energy conversion term are implemented. The first approach mirrors that of Waterhouse et al. (2014), who reported a positive linear relationship between the tidal conversion from barotropic to baroclinic wave energy and observed turbulent kinetic energy dissipation derived from shear microstructure profiles in the deep ocean. The second approach we take is perhaps more suited to shelf seas, but we retain both approaches in part to allow an intercomparison between approaches and with the deep ocean results from Waterhouse et al. (2014).

2.1. Barotropic Form Drag

The first of the two conversion formulations used here is based on the macro-scale properties of total water depth, bathymetric slope, density stratification, and mean horizontal tidal currents. Following Green and Nycander (2013) we define a stress vector describing the tidal conversion as

$$\boldsymbol{\tau}_{\mathbf{wave}} = \rho_0 \overline{\overline{\mathbf{c}}} \cdot \mathbf{u}. \tag{1}$$

Where ρ_0 is a reference density, $\mathbf{u}$ is the barotropic tidal velocity vector and $\overline{\overline{\mathbf{c}}}(x, y)$ is the internal wave drag tensor (with units ms^{-1}). We assume that τ_{wave} and $\mathbf{u}$ are parallel and can therefore replace $\overline{\overline{\mathbf{c}}}$ with a scalar coefficient formed according to the method of Zaron and Egbert (2006) and given by

$$c_{ze} = \beta h (\nabla h)^2 \frac{n_b \overline{n}}{8\pi^2 \omega}. \tag{2}$$

Where β is a scaling factor used to compensate for unresolved topography due to the horizontal resolution of the numerical model, h is the total water depth (positive) and ω is the tidal frequency. The stratification terms are formed by assuming horizontally homogeneous stratification given by $n(z) = n_0 exp(z \,/\, l_n)$ where l_n is a vertical decay constant and n_0 is a background reference stratification. n_b is then $n(z)$ evaluated at the seabed $z = -h$, and $\overline{n} = l_n n_0 [1 - exp(-h \,/\, l_n)] \,/\, h$ is the vertical average of $n(z)$. Further details of the application of these constituent parameters within this study can be found in Section 3.4

The dissipation of barotropic tidal energy per unit area as a result of the generation of internal waves over topography is then given by

$$P_{ZE} = \rho_0 C_{ZE} \mathbf{U}^2. \tag{3}$$

We use "P" here to describe the production of energy from tidal conversion, rather than "D" as in Green and Nycander (2013), in order to distinguish between the dissipative drag due to tidal conversion they describe, and pycnocline dissipation in this work, that is, observed turbulent kinetic energy dissipation.

2.2. Baines-Type Baroclinic Forcing

The second of the two conversion formulations used here is computed directly as a function of the vertical movement of isopycnal surfaces, under the influence of a barotropic tide over variable bathymetry. Following the philosophy of Baines (1982) and methodologies of Kang and Fringer (2012) and Fer et al. (2015), the barotropic to baroclinc conversion is given by:

$$P_{\rho w} = g\int_{-H}^{0}\left\langle \tilde{\rho}\mathbf{W}\right\rangle dz \tag{4}$$

for $z = 0$ at the surface and $z = -H < 0$ at the bed, and where tilde variables represent time varying fields that are reconstructed from harmonic species, as follows. $\mathbf{W}$ is the barotropic vertical velocity induced by barotropic horizontal tidal flow over an uneven bathymetry:

$$\mathbf{W} = +\frac{z}{H}(\mathbf{U}\cdot\nabla H) \tag{5}$$

In this study, the density term $\tilde{\rho}$ is reconstructed using simulated harmonics to ensure only harmonic contributions from the full hydrodynamic model are evaluated. The density term is inferred from harmonic vertical oscillations as follows. For a harmonic species (denoted with subscript ϕ and of frequency ω_ϕ) the vertical harmonic displacements are computed from the harmonic vertical velocity, w_ϕ (written in complex notation):

$$d_\phi = -\frac{iw_\phi}{\omega_\phi} \tag{6}$$

Then, the corresponding density harmonic is given by

$$\rho_\phi = \frac{\rho_0}{g}N^2 d_\phi. \tag{7}$$

These harmonic components are summed, in the usual way, to give $\tilde{\rho}$. Finally, in Equation 4, following (Guihou et al., 2018), the angle brackets ($\langle\cdot\rangle$) denote a Doodson filter (Doodson, 1921; IOC, 1985; Pugh, 1996) which is applied to hourly fields to remove the dominant diurnal and semi-diurnal tidal species.

Note that in this analysis, in contrast to the Zaron and Egbert (2006) formulation, the polarity of $P_{\rho w}$ is determined by the phase relationship between density and vertical velocity fluctuations. Negative values of $P_{\rho w}$ represent conversion from barotropic to baroclinic motions, that is, the barotropic vertical component of flow over a sloping bed being locally in phase with (or indeed generating) baroclinic vertical motion. Positive values of $P_{\rho w}$ represent conversion from baroclinic motions to barotropic flow, for example, the damping of remotely generated internal waves by an out of phase, locally generated barotropic vertical component of flow over a local sloping bed.

3. Analysis

3.1. Observational Surveys

The 18 shear microstructure and temperature data sets used in this study were collected over a 17 year period from 1996 to 2013, and span a large area of the North West European shelf, as illustrated in Figure 2. The surveys used four different instrument types, all equipped with airfoil velocity shear microstructure probes (Osborn & Crawford, 1977). Three of the types used were free falling: the FLY profiler (Dewey et al., 1987; Rippeth et al., 2003; Simpson et al., 1996), the MSS microstructure profiler (Prandke & Stips, 1998) and the VMP profiler (Palmer, Inall, & Sharples, 2013). The third platform type was a Slocum glider fitted with a Rockland Scientific Instruments Microrider (OMG) (Fer et al., 2014; Palmer et al., 2015). All of the surveys were undertaken in summer during periods of well-developed seasonal stratification, as demonstrated in Figure 3. All data sets have a total duration exceeding that of a semi-diurnal tidal period, and a sampling resolution of at least six profiles per hour. All data sets were interpolated (if required) onto a 1 m vertical grid. The majority of these data sets have been the subject of previous publications as detailed in Table 1. Those denoted with the D340 prefix and the OMG JC88 data are presented here for the first time. The D340 data sets were processed following established techniques (Prandke & Stips, 1998) and the OMG data set

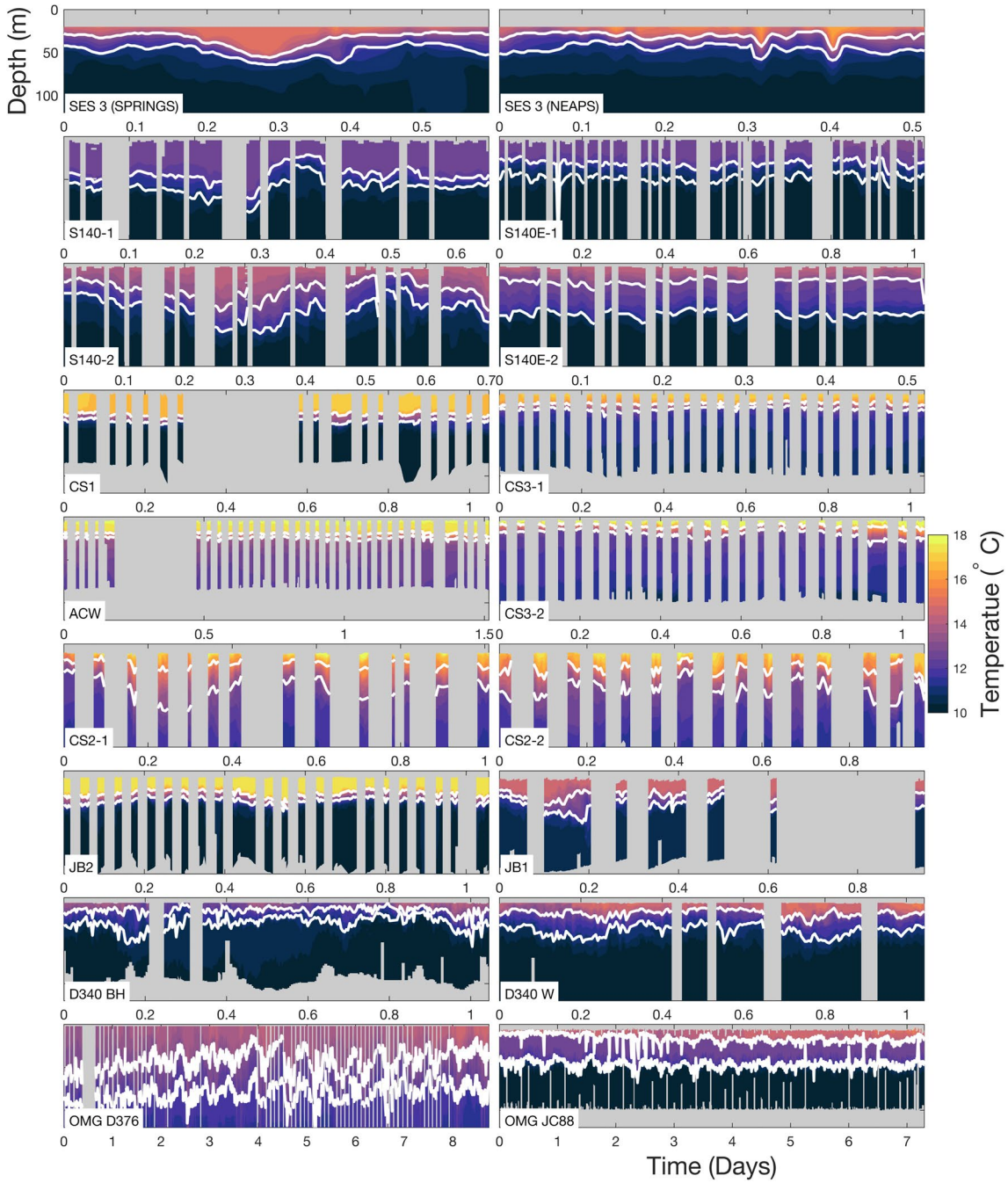

Figure 3. Temperature as function of depth and time for each microstructure survey. White lines indicate upper and lower bounds of pycnocline region, as defined by the criteria detailed in the text.

was processed following (Palmer et al., 2015). Although there are important subtleties in the three different processing methods, they all rely on the fundamental assumptions that the turbulence is isotropic and a relationship between microscale velocity shear $\frac{\partial u}{\partial z}$ and dissipation ϵ is given by

$$\epsilon = 7.5\nu\overline{\left(\frac{\partial u}{\partial z}\right)^2}, \tag{8}$$

Table 1
Microstructure Survey Location Metadata

Study name	Profiles	Duration (h)	H (m)	Year	Day	Type	∇H	U_{m2} (ms^{-1})	Reference
SES 3 (springs)	56	12.3	180	1995	233	FLY	4.08×10^{-2}	0.12	Inall et al. (2000)
SES 3 (neaps)	74	14.1	190	1995	242	FLY	3.84×10^{-2}	0.12	Inall et al. (2000)
SES 7—S140-1	106	15.6	145	1996	197	FLY	9.09×10^{-3}	0.15	Rippeth and Inall (2002)
SES 7—S140E-1	158	24.6	145	1996	198	FLY	3.63×10^{-3}	0.13	Rippeth and Inall (2002)
SES 7—S140-2	111	16.9	145	1996	204	FLY	9.07×10^{-3}	0.15	Rippeth and Inall (2002)
SES 7—S140E-2	50	12.5	145	1996	205	FLY	3.75×10^{-3}	0.13	Rippeth and Inall (2002)
CS1	132	25	80	2003	212	FLY	4.67×10^{-3}	0.31	Palmer (unpublished)
CS3-1	156	24.8	95	2003	216	FLY	2.06×10^{-3}	0.29	Palmer et al. (2008)
ACW	195	36	80	2003	218	FLY	4.46×10^{-4}	0.41	Simpson and Tinker (2009)
CS3-2	154	25.3	85	2003	221	FLY	2.06×10^{-3}	0.29	Palmer et al. (2008)
CS2-1	61	24.2	185	2005	198	FLY	2.22×10^{-2}	0.16	Sharples et al. (2007)
CS2-2	79	23.3	205	2005	203	FLY	3.59×10^{-2}	0.13	Sharples et al. (2007)
JB2	142	25.4	105	2005	211	FLY	3.53×10^{-3}	0.42	Palmer, Polton, et al. (2013)
JB1	99	22.8	105	2008	187	VMP	3.75×10^{-3}	0.43	Palmer, Inall, and Sharples (2013)
D340 BH	239	25.1	95	2009	178	MSS	9.02×10^{-3}	0.25	Inall (Unpublished)
D340 W	181	25.1	135	2009	180	MSS	3.21×10^{-3}	0.13	Inall (Unpublished)
OMG D376	777	205.3	155	2012	175	OMG	2.14×10^{-3}	0.4	Palmer et al. (2015)
OMG JC88	927	175.2	130	2013	197	OMG	8.01×10^{-4}	0.16	Palmer (Unpublished)

where ν is the kinematic viscosity of seawater. In practice, the mean shear squared term defined in Equation 8 is calculated via integration of the shear power spectrum between two wave number bounds. Wave number spectra are derived from shear time series, making a frozen field assumption. The lower and upper wave number bounds are chosen to represent the portion of the shear spectrum that can be realistically resolved by the shear probes, typically between 2 cpm and 30–50 cpm (cycles per meter) (Rippeth et al., 2003).

3.2. Pycnocline Selection Criteria

Analysis of the microstructure data set is focused on the pycnocline, so a definition must be made for a vertical region of the water column that is energetically disconnected from upper and lower boundary layer turbulence. Reliable salinity data are not available for every data set so the assumption is made that temperature serves as a reliable proxy for density. This is supported by available salinity data, and the

assumed lack of salinity control on the density structure, given both the geographical locations far from riverine inputs, and summertime conditions of all of the surveys. Hereafter, the terms pycnocline and thermocline are interchangeable. We therefore choose temperature criteria to define the pycnocline region from which ϵ populations are drawn.

The vertical structure of conservative temperature (McDougall & Barker, 2011) during each survey is shown in Figure 3. During all of the survey periods, the water column was persistently stable with respect to temperature, exhibiting a clearly identifiable thermocline. For each vertical temperature profile within each survey $T(z)$, the upper and lower boundaries of the pycnocline are defined as z_{upper} and z_{lower}, where $T(z_{upper}) = T_{min} + 0.7(T_{max} - T_{min})$ and $T(z_{lower}) = T_{max} - 0.7(T_{max} - T_{min})$ and T_{min} and T_{max} are the minimum and maximum temperatures from each profile. The upper and lower depth bounds that result from this criterion are shown as white solid lines in Figure 3.

3.3. Population Statistics and Survey Mean Values of Dissipation Rate

In order to compare microstructure derived turbulence metrics with the two forcing terms (computed for a given time and location), a single value of ϵ that best represents a temporal average must be chosen. However, there exists an inherent difficulty in doing so given that survey-wide values of ϵ are highly intermittent, and frequently span more than three orders of magnitude. In response to this challenge we follow a number of previous authors, as described in Lozovatsky et al. (2015), in choosing to view the pycnocline 1 m binned ϵ values as statistical populations. Histograms of ϵ values for which the pycnocline selection criterion described above are satisfied are shown in Figure 4. This method of selection provides large populations of ϵ values, as a value for each 1 m depth bin within the pycnocline is available. In order to relate turbulence levels to baroclinic tidal energy conversion, expressed as a vertical integral, pycnocline integrated values of ϵ are similarly vertically integrated,

$$\epsilon_{pyc} = \int_{z_{upper}}^{z_{lower}} \epsilon(z) dz. \tag{9}$$

ϵ_{pyc} values are computed for each profile of each of the 18 data sets (3,717 profiles in total). This article brings together a diverse set of time series using a number of different instrument types coming from several different data originators, therefore a unified statistical analysis of all the data is presented before presenting further analysis. To examine the statistical characteristics of each ϵ_{pyc} population we follow Lozovatsky et al. (2015) by fitting normal and generalized extreme value (GEV) distributions to populations of $log_{10}(\epsilon_{pyc})$. Both the fitted and empirical cumulative distribution functions are shown in normal probability space in Figure 5.

Also shown in Figure 5 are two representations of population averages; arithmetic means, $log10(\tilde{\epsilon}_{pyc})$ and geometric means, $log10(\hat{\epsilon}_{pyc})$. Viewing the ϵ_{pyc} populations in this way confirms that most of the ϵ populations integrated over the pycnocline exhibit a strong tendency toward log-normality. Applying a one-sample Kolmogorov-Smirnov test, only four of the 18 data sets reject the null hypothesis that the logarithm of the data comes from a standard normal distribution, against the alternative that they do not come from such a distribution (at a 5% significance level), shown in Figure 5. This strong tendency toward log normality has been found in many previous studies of turbulent dissipation derived from both temperature microstructure (Gregg, 1980; Gregg et al., 1973; Washburn & Gibson, 1984) and shear microstructure (Belyaev et al., 1975; Crawford, 1982; Oakey, 1985; Osborn, 1978; Osborn & Lueck, 1985; Palmer et al., 2015; Thorpe et al., 2008). The ϵ_{pyc} populations all exhibit deviations at their upper and lower bounds, which a GEV model does a better job of capturing, also found by Lozovatsky et al. (2015). The presence of a small number of high ϵ_{pyc} values within each population is evident in the differences between the geometric and arithmetic means, with the former being significantly smaller in each case. Overall, this statistical analysis provides assurance of the data quality across the wide variety of data sets used, demonstrating also that all ϵ distributions lie well above instrument detection limits of between $\sim 1 \times 10^{-9} Wm^{-3}$ (MSS, FLY) and $\sim 1 \times 10^{-10} Wm^{-3}$ (VMP, OMG).

A geometric mean is the favored option for representing the mean of a skewed distribution (identical to the arithmetic mean of the log transformed values). Given we wish to best characterize the entirety of each microstructure survey period with a single value, and not to be biased toward a small number of high

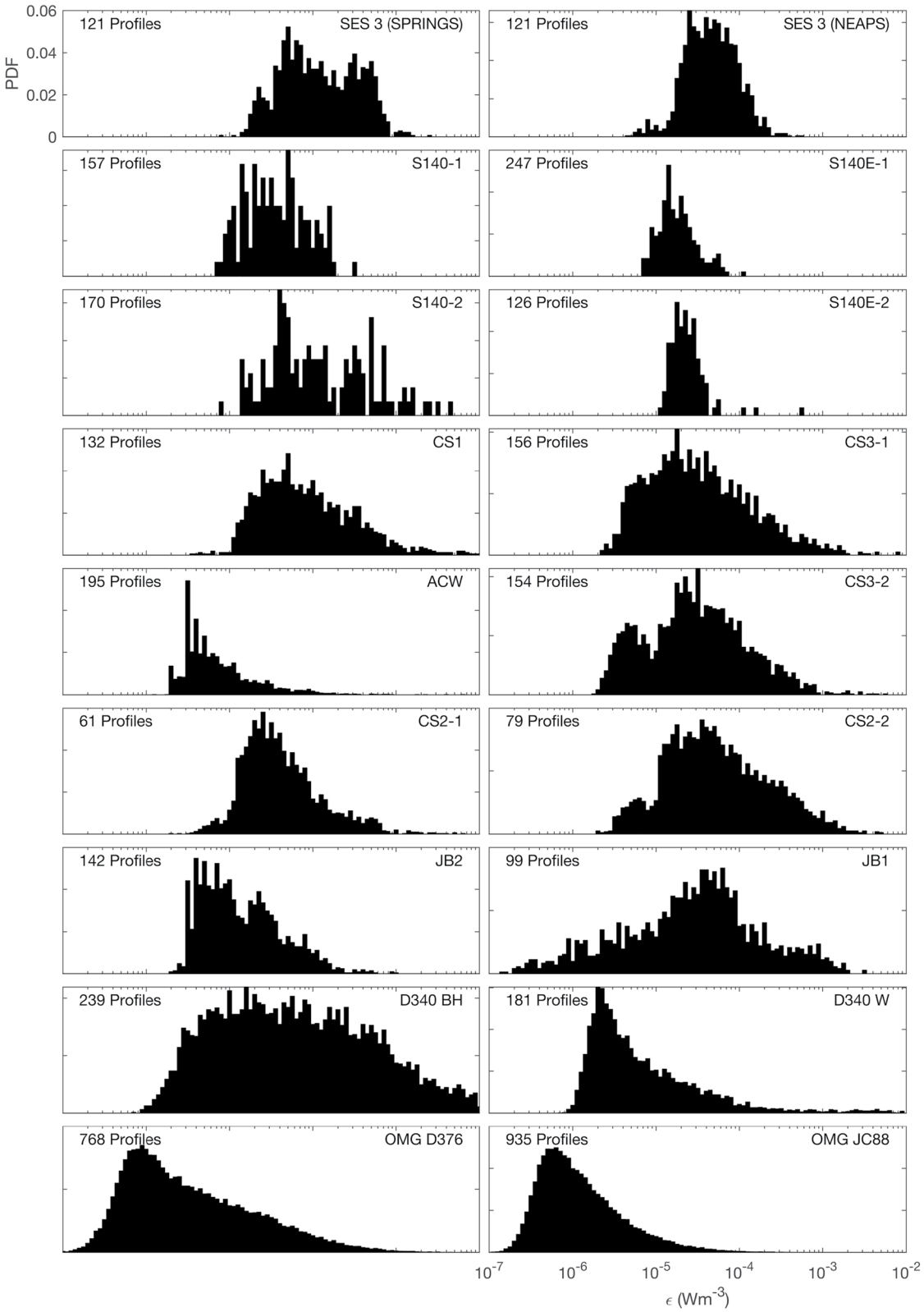

Figure 4. Histograms of ϵ observations for each of the microstructure surveys. Histograms are constructed by first linearly interpolating each microstructure profile onto 1 m depth intervals. The values for which the pycnocline selection criterion described in the main text satisfied are then treated as independent samples.

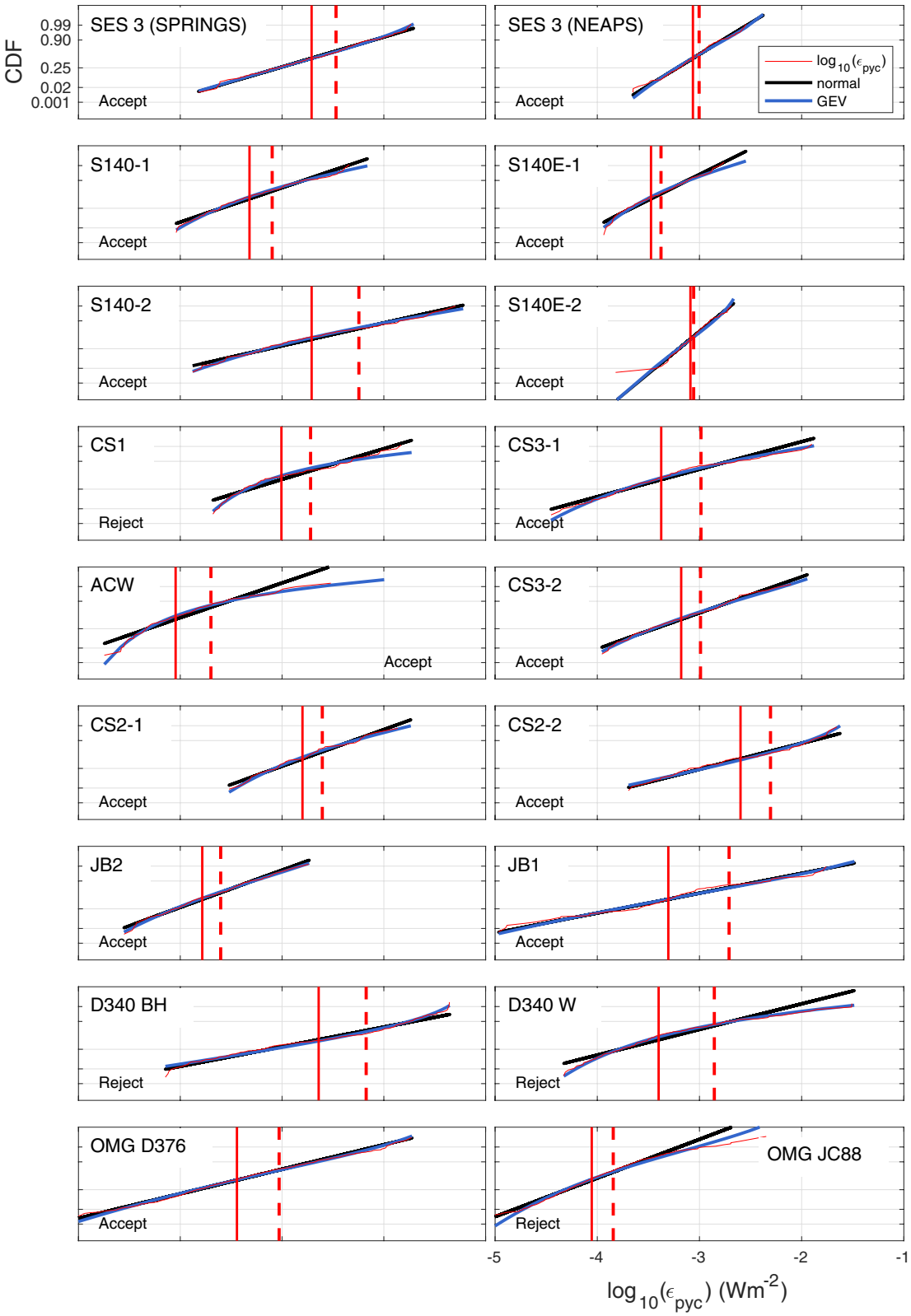
CDF
0.99
0.90
0.25
0.02
0.001
SES 3 (SPRINGS)
Accept
SES 3 (NEAPS)
Accept
log10(ϵpyc)
normal
GEV
S140-1
Accept
S140E-1
Accept
S140-2
Accept
S140E-2
Accept
CS1
Reject
CS3-1
Accept
ACW
Accept
CS3-2
Accept
CS2-1
Accept
CS2-2
Accept
JB2
Accept
JB1
Accept
D340 BH
Reject
D340 W
Reject
OMG D376
Accept
OMG JC88
Reject
-5
-4
-3
-2
-1
log10(ϵpyc) (Wm-2)

Figure 5.

values, we choose the geometric mean with which to compare to the macro scale barotropic to baroclinic conversion terms. For completeness, the same analysis was undertaken using the arithmetic mean, with the difference not changing the overall conclusions as detailed in Section 3.5.

Finally, in order to compare the observed mean dissipation rates with the tidal forcing terms (following, e.g., Waterhouse et al., 2014), an adjustment is made to account for the fraction of turbulent energy already converted to increased water column potential energy,

$$D_\epsilon = \frac{\hat{\epsilon}_{pyc}}{(1-\Gamma)} \tag{10}$$

where D_ϵ is the total energy dissipation rate within the pycnocline and $\hat{\epsilon}_{pyc}$ is the geometric mean of ϵ_{pyc}. Γ is the proportion of energy that acts to change the potential energy of the water column through mixing, $(1-\Gamma)$ is the proportion that dissipates as heat, and is the proportion actually observed by the shear microstructure method. A canonical value of $\Gamma = 0.2$ (Osborn, 1980) is used. A sensitivity analysis is presented in Section 3.5, where upper and lower bounds on D_ϵ are computed using a range of values for $\Gamma = 0.05 - 0.25$, demonstrating a relatively small impact on the final comparison between conversion and dissipation.

3.4. Simulation Derived Barotropic to Baroclinic Energy Conversion

As described in Section 2, the two baroclinic forcing terms are computed using output from the high resolution AMM60 NEMO configuration covering the North West European Shelf and Atlantic margin (Guihou et al., 2018). The model output used for this study is centered around August 24, 2012. The reason for selecting one particular summertime period, rather than the actual times of each observational data set is rather prosaic: model output for the time period of the earliest observational data sets is not available. Nevertheless, since we are dealing with a system dominated by tidal currents and seasonal stratification, both of which are largely deterministic and repetitive, the use of a representative summer period, though a nonideal necessity, is deemed necessarily informative for our purposes since spatial distribution and range of forcing values is the focus. To demonstrate this, profile comparisons between the 1m depth binned survey averaged observed stratification and co-located 5-day mean modeled stratification centered on the 24th of August 2012 are shown in Figure 6 for each data set. Buoyancy frequency is computed from temperature profiles with a constant absolute salinity value of 35 for the observations, and both for this same constant salinity value and the actual modeled salinity for the model output. Broadly speaking, the modeled summer 2012 stratification matches that observed. There are of course differences between model and observed stratification, particularly severe at site D340BH, which is close to the poorly resolved topography of Barra Head. An investigation into the sensitivities of AMM60's ability to reproduce observed stratification is presented elsewhere (Luneva et al., 2019), and is not the focus here.

Values of the Baines type forcing, $P_{\rho w}$, are computed "offline" using tidal harmonics of density and velocity fields. Computing the barotropic form drag term, P_{ZE}, requires the constituent terms describing the tidal velocity, the bathymetric gradient, the stratification and a scaling factor β. The tidal velocity vector U, is the harmonically derived current amplitude of the M2 tidal constituent. The bathymetric gradient term is computed using the native horizontal resolution of the model bathymetry. In terms of stratification, we follow Green and Nycander (2013) in applying a vertical exponential profile, and determine the reference stratification N_0, and decay length scale, Ln appropriate for this shelf seas application. These terms are derived by computing profiles of $N(z) = N_0 exp(z \,/\, L_N)$, with values of N_0 and L_N that yield $N(z)$ profiles that best match each observational profile from pycnocline downwards. This results in values of N_0 ranging from $0.004\ s^{-1}$ to $0.03\ s^{-1}$ with a mean value of $N_0 = 0.015 s^{-1}$, and values of L_N ranging from $20m$ to $55m$ with a mean value of $37m$, shown in Figure 6. The average values of N_0 and L_N are then used to compute the P_{ZE} conversion term for the entire domain, applying a horizontal scaling constant scaling $\beta = 50 \,/\, (7.5^2)$.

Figure 5. Cumulative distribution functions of pycnocline integrated TKE dissipation rate, $log10(\epsilon_{pyc})$ for each microstructure survey are shown in red. The arithmetic, $log10(\tilde{\epsilon}_{pyc})$ and geometric, $log10(\hat{\epsilon}_{pyc})$ means are shown in red dashed and red solid vertical lines, respectively. A fitted normal and generalized extreme value distribution are shown in black and blue, respectively. Each panel is annotated with whether the null hypothesis that data comes from a standard normal distribution, against the alternative that it does not come from such a distribution, is accepted or rejected at a 5% significance level, using a one-sample Kolmogorov-Smirnov test.

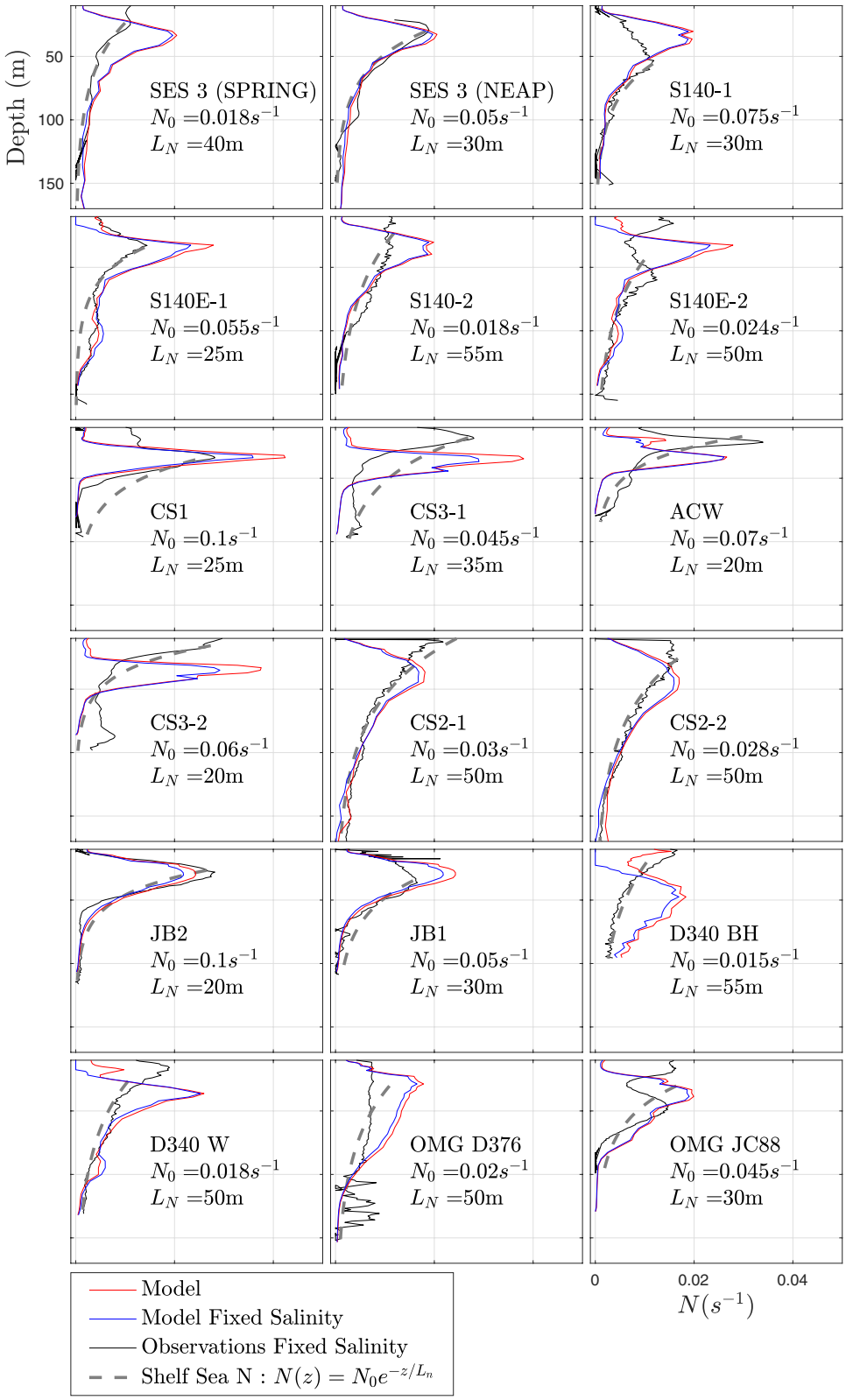

Figure 6. $N(z)$ profiles for each microstructure survey location. Numerical model derived values are computed using both model salinity (red) and a fixed (35 psu) salinity (blue). Values for observations are computed with the same fixed salinity (black). Exponential shelf sea $N(z)$ profiles computed with L_N and N_0 values chosen to best match the observational values from the bed to the center of the pycnocline are also displayed (gray dashed).

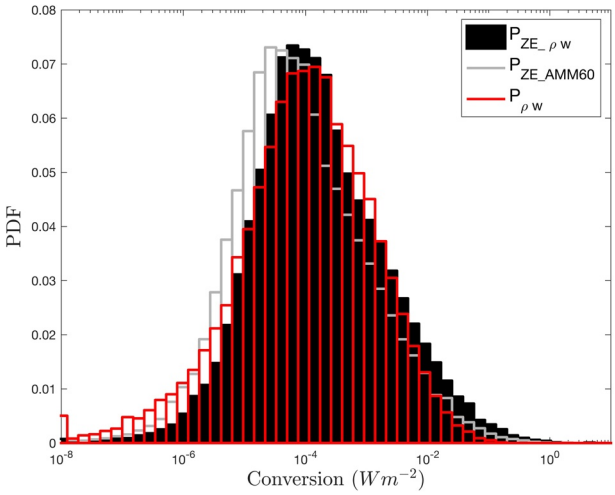

Figure 7. Histograms of tidal conversion terms computed over the entire domain shown in Figure 8. $P_{\rho w}$ is shown in red. P_{ZE_AMM60} shown in gray, represents P_{ZE} evaluated with observationally tuned N_0 and L_N values and AMM60 model grid resolution tuned β. $P_{ZE\_\rho w}$ shown in black represents P_{ZE} evaluated with shelf sea observationally tuned N_0 and L_N, and β tuned to best match the values of $P_{\rho w}$.

This value for β accounts for the ratio of the horizontal resolution of the AMM60 model (1 / 60°) to the 1 / 8° resolution of the model used in Green and Nycander (2013), where they apply $\beta = 50$. Histograms of P_{ZE} and $P_{\rho w}$ (Figure 7) show great similarity in shape, with the distribution of P_{ZE} offset toward smaller values than $P_{\rho w}$ by a factor of approximately two. The value for β, a free parameter, is then tuned so that both populations align, giving a tuned value of $\beta = 100 / (7.5^2)$. This re-tuning of P_{ZE} is returned to in the discussion.

Maps of both $P_{\rho w}$ and $P_{ZE\_\rho w}$, referred to hereafter simply as P_{ZE}, for regions within the model domain with total water depth shallower than 300m are shown alongside a data density binned scatter plot in Figure 8. Conversion values for later comparison with $\hat{\epsilon}_{pyc}$ of both $P_{\rho w}$ and P_{ZE} are then extracted, and arithmetically averaged within a radius of 5 km from the location of each of the observational ϵ data sets.

3.5. Conversion Rates Versus Pycnocline-Averaged Dissipation Rate

The model derived tidal energy conversion terms, $P_{\rho w}$ and P_{ZE}, both demonstrate a positive and approximately linear relationship with the observationally derived dissipation term D_ϵ, in loglog space. A linear regression model is used to determine the gradient of the relationship between tidal conversion and pycnocline dissipation in loglog space. The resulting best fit lines in linear space relate to: $D_\epsilon = aP^b$. For $P_{\rho w}$, $a = 4.8 \times 10^{-3}$ and $b = 0.28$. For P_{ZE} , $a = 8.1 \times 10^{-3}$ and $b = 0.33$. Both of the conversion terms versus dissipation have a gradient conforming approximately to a one-third power law relationship between production and dissipation (Figure 9). The root mean standard error of the regression is computed and shown, demonstrating that to within one standard error the slope of the linear relationship is significantly less than one. Horizontal bars representing the minimum and

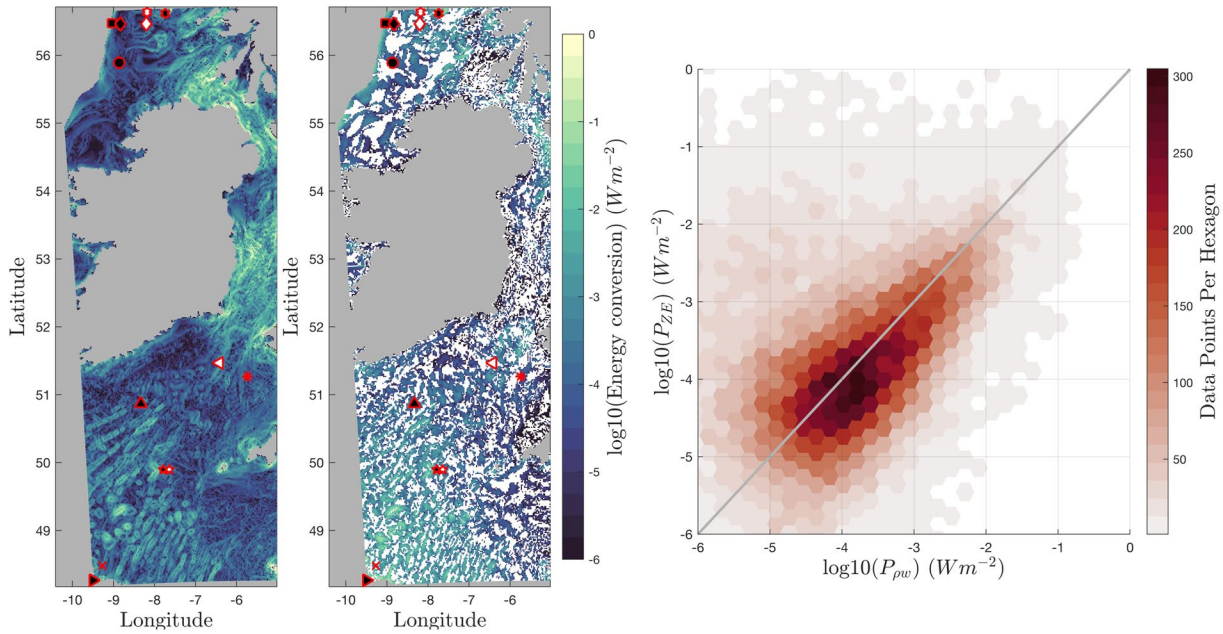

Figure 8. Left: Map of P_{ZE}. Middle: Map of the modulus of the negative values of $P_{\rho w}$, positive values of $P_{\rho w}$ are shown in white. Markers in maps display survey locations (legend shown in Figure 2). Right: Data density plot of P_{ZE} as a function of the modulus of the negative values of $P_{\rho w}$.

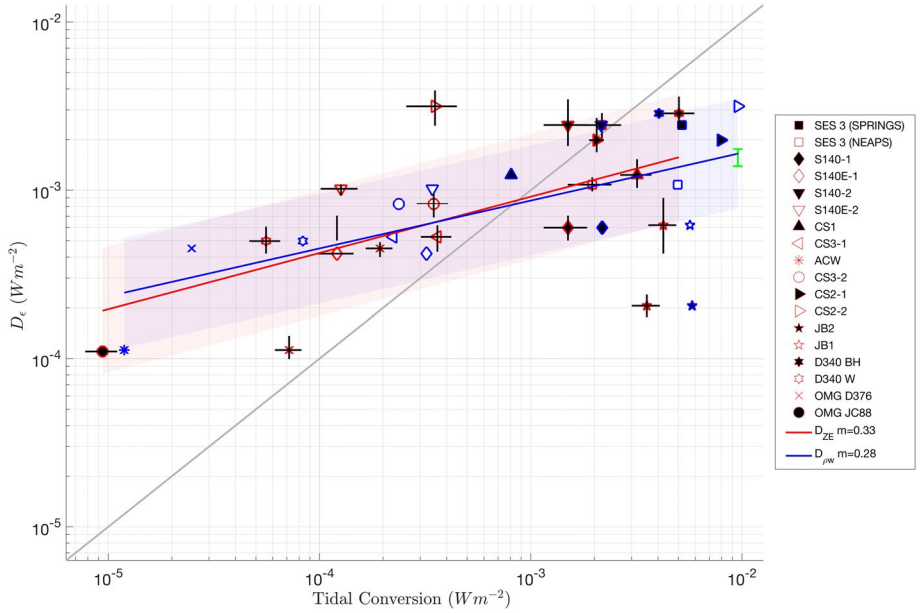

Figure 9. D_ϵ, as a function of tidal conversion estimates, calculated as P_{ZE} (red markers) and $P_{\rho w}$ (blue markers). D_ϵ values are geometric temporal means, P_{ZE} and $P_{\rho w}$ values are arithmetic spatial means from within a 5 km locus of each profiling location. $P_{\rho w}$ values are the modulus of those values which are negative, with those that are positive (OMG JC88) omitted. The red and blue solid lines display the results of a simple linear regression of the logarithm of the D_ϵ and tidal conversion values. The fitted gradients are shown in the legend and the shaded areas bound the upper and lower root mean standard error of the linear fit to the data. Gray line shows a linear one to one relationship. Green lines demonstrate the upper and lower values of D_ϵ when a Γ of between 0.05 and 0.25 is applied. The black vertical lines represent the upper and lower 95% bootstrap confidence intervals. The black horizontal lines demonstrate spring-neap variation by bounding the minimum and maximum P_{ZE} when computed with both M2 and S2 tidal constituents.

maximum values of P_{ZE} when computed with both the M2 and S2 tidal constituents also demonstrate that within this variability the gradient still remains robustly less than one.

The analysis was repeated using arithmetic mean values of dissipation. The geometric mean values are systematically lower, Figure 5. But critically, the gradients of observed dissipation to conversion terms are very similar, with values of $\partial D_\epsilon \,/\, \partial P_{ZE} = 0.37\ (0.33)$ and $\partial D_\epsilon \,/\, \partial P_{\rho w} = 0.23\ (0.28)$ (geometric means in brackets). The gradient suggests a general imbalance between local barotropic to baroclinic conversion and local pycnocline dissipation. The imbalance changes sign at $\sim 8 \times 10^{-4} Wm^{-2}$, increasing as the energy entering the baroclinic wavefield increases further, following a power law of approximately one-third. This is an interesting result, and suggests that at higher conversion rates, the energy flux divergence of the internal wavefield due to energy dissipated *within the pycnocline* does not "keep-up" with increasing energy input into the internal wavefield.

Also noteworthy is the statistically significant result that pycnocline dissipation is higher than estimated conversion at low conversion rates (and, conversely, lower at high conversion rates as noted). This is consistent with the notion of an omnipresent internal wave "background" energy level, indicating the influence of other energy sources such as the wind or remotely generated internal waves. Locally, we may therefore expect that in low conversion regions, dissipation levels measured in the pycnocline will be greater than the local generation rate, because of wind or baroclinic energy radiating into the measurement zone from non-local sources.

Finally, with reference Figure 9, integrated over the full range of conversion space, that is from 1×10^{-5} to $9 \times 10^{-3} Wm^{-2}$, pycnocline integrated ϵ accounts for only ~25% of conversion.

3.6. Pycnocline Versus Bottom Boundary Layer Dissipation

To examine in more detail the apparent one-third power law relationship between tidal energy conversion and pycnocline integrated dissipation, and the overall ~75% dissipation deficit (Figure 9), we look first with-

in the baroclinic wave energy budget. The most obvious candidate mechanism is that of local wave energy dissipation within the bottom boundary layer. Since dissipation in the bottom boundary layer is known to exceed pycnocline dissipative energy losses in nonlinear internal waves (NLIWs), and more generally in internal tides (Inall & Rippeth, 2002; Inall et al., 2000). Does the internal wave energy lost to bottom friction increasingly dominate the internal wave energy budget as wave amplitude, A_{bc} increases? This is a reasonable question to ask, since A_{bc} is expected to increase with increasing conversion rate (unless the wavefield is amplitude saturated), though no simple expression directly relates A_{bc} to conversion.

Tidal conversion puts energy into baroclinic motions, in which turbulence may dissipate energy within a sheared pycnocline and within a turbulent bottom boundary layer through frictional bottom boundary drag acting on the near bed velocity. Full-depth turbulence observations are not available for many of the data sets. Even in data sets which do fully capture the bottom boundary layer, separate attribution of observed bottom boundary turbulence to barotropic tidal flow and to that generated by baroclinic motions is nontrivial, see for example the discussions in Inall et al. (2000) and Inall and Rippeth (2002). Barotropic and baroclinic tides, by their very nature, are phase locked with the same fundamental frequency, but their phase difference is spatially varying due to the large difference in wavelength of barotropic and baroclinic tides (factor of around 20, varying with stratification). This picture of spatial phase differences is complicated by time variation in barotropic forcing (e.g., spring/neap cycle) which may result in remotely forced baroclinic energy phase-shifted from the local barotropic signal (Nash, Kelly, et al., 2012; Nash, Shroyer, et al., 2012), which in turn may result in more energetic baroclinic waves at a neap tide, rather than a spring tide, for example, Inall et al. (2000). A further complication may result from storm-forced variations in stratification which have been show to modify baroclinic wave energy flux across a wide shelf (Stephenson et al., 2015). For all of these reasons, and possibly others, it is not possible to look to the ϵ observations or AMM60 estimations of ϵ to determine the relative dissipative contributions of pycnocline and bottom friction as a function of local baroclinic wave amplitude, A_{bc}. We can, however, turn to some commonly used parameterisations of pycnocline dissipation to examine this question.

3.7. Parameterized Models of Boundary and Internal Dissipation Rates

The simplest approach is to first consider the relative scaling of internal and boundary friction. The latter, as demonstrated for example in Simpson et al. (1996), is accurately approximated as

$$\epsilon_{BBL}(t) = \rho C_d U_L^3(t). \tag{11}$$

Where ρ is near bed density and C_d is a turbulent drag coefficient, usually taken to be 2.5×10^{-3}. Treating the water column initially as a two layer fluid with the upper and lower layers of thickness, H_U and H_L, which are later estimated from the vertical position of the maximum in the first mode vertical velocity structure, upper and lower layer baroclinic velocity amplitudes are related to A_{bc} by

$$U_U = \left(A_{bc} \,/\, H_U\right) c_{bc} \quad \text{and} \quad U_L = \left(A_{bc} \,/\, H_L\right) c_{bc}. \tag{12}$$

Where A_{bc} is the first mode internal wave amplitude, and U_U and U_L the upper and lower layer baroclinic velocities, and c_{bc} the wave phase speed (which later is also determined from the internal wave eigenvalue problem). Energy dissipation in the bottom boundary layer therefore scales as $\epsilon_{BBL} \propto A_{bc}^3$. Internal wave shear, S, at the interface scales linearly as $S \propto A_{bc}$, where

$$S = (U_U - U_L) \,/\, \Delta Z, \tag{13}$$

with ΔZ a finite measure of pycnocline thickness. Various empirically derived fine-scale parameterizations of pycnocline dissipation rate have been proposed in the literature. Here, we examine three commonly used versions, as discussed in Palmer, Polton, et al. (2013): denoted Gregg (Gregg, 1989); KWB (Kunze et al., 1990); and MG (MacKinnon & Gregg, 2003). The Gregg parameterization is defined as

$$\epsilon_{Gregg} = \alpha_G \frac{\langle N^2 \rangle}{N_0^2} \frac{S^4}{S_{GM}^4}. \tag{14}$$

Where α_G scales ϵ_{Gregg} to best match observed values, N_0 represents background levels of pycnocline N and angled brackets denote temporal averaging. S_{GM} is the Garrett and Munk (1975) model of the oceanic

internal wave shear spectrum, which as shown by Gregg (1989) can be estimated as a function of the local stratification, given by $S_{GM} = 1.91 \times 10^{-5}(N / N_0)^2$. The KWB parameterization is defined as

$$\epsilon_{KWB} = fr.\Delta z^2 \left\langle \left(\frac{S^2 - 4N^2}{24} \right) \left(\frac{S - 2N}{4} \right) \right\rangle. \quad (15)$$

Where fr represents the fraction of the water that is thought to be gravitationally unstable. The Δz term is defined in Kunze et al. (1990) to be the region of the water column where $S > 2N$ that is, $Ri <= 0.25$. Finally, the MG parameterization is defined as

$$\epsilon_{MG} = \alpha_{MG} \frac{N}{N_0} \frac{S}{S_0} \quad (16)$$

where α_{MG} is another free scaling parameter, and S_0 represents background levels of pycnocline S.

Reference is made here to the Gregg and KWB scalings for context, but are excluded from more detailed analysis for the following reasons. Both the Gregg and KWB scalings rely on resolving higher mode waves, while our analysis utilizes the first mode solutions only. The Gregg parameterization explicitly excludes the tidal contribution, the focus of this study, and the KWB scaling relies on an ability to resolve to a critical Richardson number, which is not possible with the methods here. Furthermore, for a given stratification, $\epsilon_{Gregg} \propto A_{bc}^4$, $\epsilon_{MG} \propto A_{bc}$, and $\epsilon_{KWB} \propto A_{bc}^3$. Recalling that $\epsilon_{BBL} \propto A_{bc}^3$, it is evident that only the MG parameterization has a lower power law scaling for pycnocline dissipation compared to BBL dissipation, that is, MG has pycnocline dissipation linearly proportional to shear. KWB has cubic power dependence for pycnocline dissipation, same as BBL dissipation, while Gregg has a forth power dependence. On the basis of these notes, we would anticipate that only the MG parameterization will mirror the one-third power law behavior seen between observed dissipation and tidal conversion.

To make a direct comparison between BBL versus pycnocline dissipation and tidal conversion (rather than the baroclinic wave amplitude, as above), the MG mixing parameterization scheme is evaluated within an iterative approach to estimate the predicted values of pycnocline and bottom boundary layer turbulent dissipation rates for each of our survey locations. In order to compute the M2 tidally averaged layer-wise velocities, first mode internal wave eigenvalue solutions are computed to give the phase speed, c_{bc} (solving the Taylor-Goldstein equation) using the same AMM60 output presented earlier used in computing the tidal conversion terms. Velocity shear is then computed as $S = \langle U_U - U_L \rangle / \Delta_{pyc}$. The stratification term is taken as the maximum value of buoyancy frequency, N, found within each of the modeled density profiles. For consistency (MacKinnon & Gregg, 2003) we apply regionally appropriate scaling constants $S_0 = N_0 = 1.5 \times 10^{-2} s^{-1}$, and α_{MG} equal to $6.9 \times 10^{-7} Wm^{-3}$.

This approach allows the first mode internal wave amplitude, A_{bc}, to be determined iteratively for each data set as follows: The total internal wave dissipative energy loss may be expressed as a function of internal wave amplitude (A_{bc}) as $\epsilon_{total}(A_{bc}) = \epsilon_{bbl}(A_{bc}) + \epsilon_{MG}(A_{bc})$. These evaluations for the total dissipation are iterated across a range of synthesized internal wave amplitude A_{bc} space (from 0.1 to 75 m) in order to minimize the difference between ϵ_{total} and the calculated tidal conversion, P_{ZE} at each survey location. This procedure forces a convergent solution for A_{bc} for each data set, and hence for $\epsilon_{total}(A_{bc})$ and its two constituent terms, $\epsilon_{total}(A_{bc})$ and $\epsilon_{MG}(A_{bc})$, as a function of P_{ZE}. The results are as shown in Figure 10. In essence, this method is used to reveal the partition, as a function of tidal conversion, between total TKE dissipation in the bottom boundary layer (given by a cubic dissipation law) and in the pycnocline as given by the MG parameterization. If pycnocline dissipation scales as the lower layer velocity (as in the MG parameterization), then one anticipates a one-third power law relationship between pycnocline dissipation and conversion. This is very nearly the case with a gradient of parameterized pycnocline dissipation to tidal conversion of 0.4. We acknowledge that the choice of scaling factor applied in the MG parameterization in Equation 16, may lead to some of the disparity between this and our observed D_ϵ. The absolute value of pycnocline integrated dissipation derived from this parameterization is much lower than observed, but an absolute comparison is not our focus. Rather we are interested in the one-third scaling with conversion which is invariant to choice of the scaling factor.

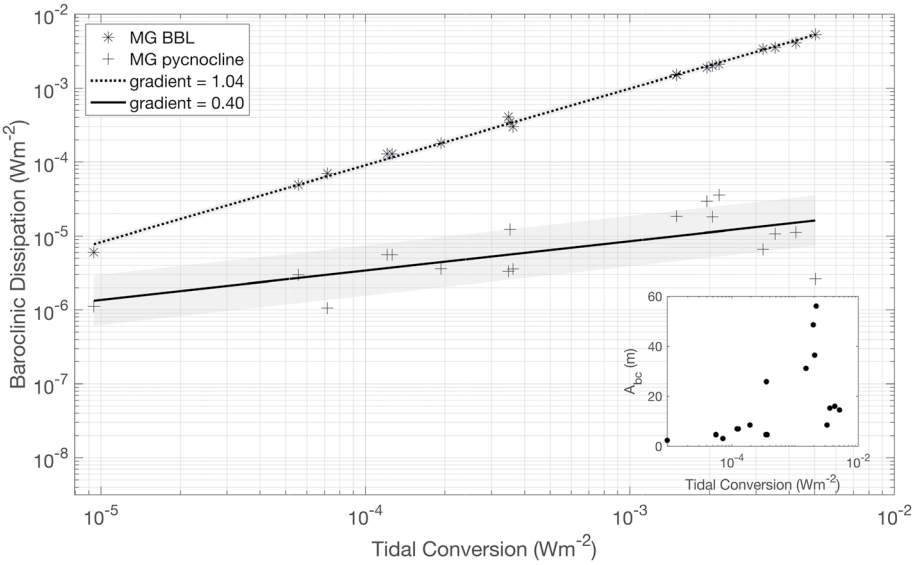

Figure 10. Optimized ϵ_{bbl} (stars) and ϵ_{MG} (crosses) as a function of P_{ZE} for each micro-structure survey location, where the optimal value of A_{bc} (inset) is found to be less than 75 m. The dotted and solid lines display the results of a simple linear regression of the logarithm of the baroclinic dissipation and tidal conversion values. The fitted gradients are shown in the legend and the shaded areas bound the upper and lower root mean standard error of the linear fit to the data.

4. Discussion

The positive relationship between pycnocline integrated ϵ and both tidal conversion estimates is perhaps unsurprising, though it is noteworthy as a general observation encompassing a large number of independent data sets covering a broad geographic range and a correspondingly wide range of dissipation and conversion values. That the relationship is not one-to-one does suggest that the concept of shelf seas internal wavefield being in some sense "saturated" (e.g., Sherwin, 1988; Thorpe & Liu, 2009) may be more nuanced, and strongly dependent on external interaction of the internal wavefield with a boundary. In that last statement, we interpret "saturated" to mean that the local rate of energy input into the internal wavefield equals the local rate of energy loss with minimal or no local growth in wave amplitude, noting also that the term "saturated" does not have a consistent definition in the literature.

If internal wave energy loss (dissipation) is occurring only in the stratified portion of the water column (e.g., as implicit in Thorpe & Liu, 2009), then increased energy input (i.e., conversion) would scale linearly with wave energy loss within the stratified portion of the fluid, which is not as observed here. The example given in Thorpe and Liu (2009) most closely related to internal waves in a shelf sea environment is the stratified and tidally swept Clyde Sea. Using an inviscid interpretation, they suggest the system is highly unstable (saturated, in some sense), and yet it has been demonstrated that internal wave energy loss there is dominated by friction in the bottom boundary (Inall & Rippeth, 2002). It is unclear how the interpretation of stability and saturation would change if the inviscid assumption were relaxed.

That we do see pycnocline dissipation increasing monotonically, but not proportionally with conversion is, however, consistent with the notion that the shelf seas pycnocline is maintained in a continual state of marginal stability (and by that we mean a bulk Richardson Number ~1), by the BBL and/or wind/convection (Lincoln et al., 2016). Following this line of reasoning, even a small amount of additional energy given to the internal tide (i.e., greater conversion) gives rise to increased wave amplitude and therefore greater shear instability (and enhanced dissipation) internally and at the boundary, draining energy directly from the internal tide to mixing (change of water column potential energy) and to heat. The additional result here that pycnocline integrated ϵ is higher than estimated conversion in locations of low conversion rates is also consistent with the notion of marginal stability: in regions of locally lower conversion, dissipation exceeds

the energy locally entering the baroclinic wavefield because of the ubiquitous background baroclinic energy density from energy radiating into that region from non-local sources.

One of the two conversion estimates, P_{ZE}, contains a free tuning parameter, β. Using the deep ocean tuning (Green & Nycander, 2013), appropriately adjusted here for differing model resolution, results in P_{ZE} values that are systematically smaller than $P_{\rho w}$ (Figure 7). For application to the NW European shelf seas $P_{\rho w}$ is used to provide a new tuning for P_{ZE}, by adjusting β to force P_{ZE} to match $P_{\rho w}$. This approach is justified on the grounds that P_{ZE} contains a free parameter and $P_{\rho w}$ does not, and there is no way to assess errors associated with the directly diagnosed $P_{\rho w}$. Tuned in this manner, P_{ZE} provides a relatively simple method to calculate shelf seas tidal conversion using only knowledge of topography, barotropic tide and stratification, without recourse to a 3D, high resolution, baroclinic hydrodynamic numerical model.

Tuning β does not affect the power law relationship with pycnocline integrated ϵ, and both conversion formulations exhibit similar power law relationships to pycnocline integrated ϵ. Both exhibit a gradient on a loglog scale of ≈ 0.3 which in linear space relates to $\epsilon \propto Conversion^{1/3}$. This is an important result, though we are cautious in inferring anything about both conversion estimates having the same power law, since they are not completely independent (both using AMM60 velocity and stratification fields), and we acknowledge we are unable to assign error estimates to either of the conversion estimates.

The approximate one-third power law, shown to be robustly less than one, states that for every factor of 10 increase in barotropic energy conversion (perhaps near some steep topography, or region of strong barotropic tide), will result in only an approximate doubling in pycnocline dissipation (and hence associated vertical mixing and vertical heat/nutrient fluxes). This does not necessarily suggest a less-than-expected change in energy flux divergence in the baroclinic wavefield; just that we do not see a one-to-one relationship between change in energy input to the baroclinic tide (i.e., conversion), and a change in energy dissipated within the thermocline. It is also acknowledged that there is considerable scatter to the observations, and the observed power law fit could be between one-quarter and one-half. For example, observing that P_{ZE} is proportional to $(\nabla H)^2$ a one half power law would be consistent, to first order, with dissipation varying with ∇H, which is not unreasonable given that internal tide amplitude will scale as the dot product of barotropic tidal velocity and the local bathymetric slope. This reasoning, though, speaks only to the source of the energy conversion, it does not address wave energy flux divergence partitioning between pycnocline and other forms of dissipation, for example that occurring in the bottom boundary layer. It should also be re-stated that wind driven inertial energy has not been considered, and both conversion estimates are linear, that is, they do not account for supercritical flow over topography.

The approximate one-third power law relationship raises questions about possible mechanisms for dissipating the "excess" baroclinic energy conversion compared with pycnocline dissipation noted at higher conversion rates. BBL dissipation was selected and evaluated as the primary candidate mechanism. There are though (at least) three candidate processes, the second and third of which deserve some comment:

1. Local BBL dissipation. Supported by previous work (Inall et al., 2000; MacKinnon & Gregg, 2005; Rippeth, 2005) showing between 60 – 80% of IW energy to be dissipated in the BBL;
2. Remote internal wave breaking, or energy absorption into shelf seas fronts;
3. Nonlinear interaction with barotropic tides.

An explanation that invokes remote dissipation must counter the criticism that any point in the shelf seas will contain both locally and remotely generated internal waves, as we have illustrated with pycnocline integrated ϵ exceeding conversion in low conversion locations. Remote dissipation hot spots, such as shoaling topography and fronts between stratified and well mixed water remains remain free of this criticism. Since BBL dissipation associated with NLIWs is known to exceed that in the pycnocline (Inall et al., 2001) and no measurement in our database were collected in fronts or over steep slopes, we have focused our attention on BBL dissipation.

There is a fundamental issue in trying to separately attribute dissipation in the BBL arising from internal tides and that arising directly from the barotropic tide. This issue is particularly acute when barotropic tidal velocity magnitude is similar to the internal tide induced velocity, as is the case on the NW European shelf. Barotropic and baroclinic tides are phase locked at any given location, their velocities above the boundary

will constructively or destructively interfere (or anything in between) in a consistent fashion at any given location (see discussion in Inall et al., 2000). The cubic dependence of BBL dissipation on near boundary velocity will therefore give rise to nonlinear, spatially varying interactions between barotropic and baroclinic signals, even on a flat seabed. The introduction of spatially varying topography further complicates the picture. The overall notion, therefore, is that dissipation in the BBL caused by barotropic and baroclinic motions is intrinsically inseparable. For example, high conversion rates are associated with large barotropic tidal velocities, and thus a cubic increase in BBL dissipation. This in turn might be viewed as creating a more viscous lower boundary over/through which the internal wave motions must propagate. This may consequently damp the internal tide/wavefield in a nonlinear fashion, thereby reducing wave amplitude, shear and pycnocline mixing. This line of reasoning, though somewhat speculative has, to the best of our knowledge received little attention in the literature and is mentioned in only a small number of studies (e.g., Inall et al., 2000; MacKinnon & Gregg, 2005). Bearing this caveat in mind, we have nonetheless considered the baroclinic motions in isolation of the barotropic tidal velocities, leaving analysis of their interaction for future study.

The simple scaling arguments of Section 3.6 suggest that the observed power law (Figure 9) is consistent with a linear dependence between pycnocline dissipation and baroclinic shear. It follows that an overall balance between conversion and dissipation is possible and consistent with this broad collection of 18 observational data sets of pycnocline dissipation. As already noted, the NW European shelf sea is often considered to be in a general state of marginal stability (with respect to a bulk Richardson Number - noting this to be a generalized statement, and stability thus defined will vary greatly in time and space). The success of the MG scheme in reproducing the observed power law dependence of pycnocline dissipation on tidal conversion is consistent with ϵ_{pyc} scaling with the product of N and S, in the sense that the shelf sea pycnocline sits at all times close to $Ri_{bulk} \sim 1$. Thus additional input in S will increase mixing, and any increase of N will result in greater baroclinic conversion and hence increased mixing (rather than stabilization of an unforced system).

As a final point of discussion, the one-third relationship reported here is different to the generalized relationship found by Waterhouse et al. (2014), who report $\epsilon \propto Conversion$. However, when Waterhouse et al. (2014) extract just internal tides (i.e., baroclinic conversion forcing) they find what appears to be a similar one-third power law (see left panel of Figure 4 in Waterhouse et al., 2014). This is a surprising observation. It is improbable that in the open ocean baroclinic tides dissipate largely through bottom friction, disproportionately increasing as a function of energy conversion into the baroclinic wavefield. A more likely interpretation is that the similarity in slope is a coincidence, and that the deep ocean sub-unity gradient reflects the widely accepted notion that the majority of deep ocean internal wave energy is dissipated at the ocean boundaries, including the marginal shelf seas, or lost to other processes, for example, acceleration of mean flow through wave-current interaction.

5. Conclusions

Whichever way one views the discussion above, we are left with two robust statements: (a) pycnocline dissipation is less than conversion at high local conversion rates and greater than for low local conversion rates; (b) the scaling of local pycnocline dissipation to local conversion rate follows an approximately one-third power law. Further, we suggest that these statements are consistent with an overall balance between conversion and dissipation only if one considers wave-induced dissipation within the BBL. At low conversion rates, local dissipation may exceed local conversion due to a remotely generated background baroclinic wave energy density, or a contribution from another source, that is, the wind. As conversion increases, there is a proportionate rise in the flux divergence of internal wave energy through increased BBL dissipation. However, as conversion increases there is *not* a proportionate rise in the flux divergence of internal wave energy through internal friction. Therefore, local diapycnal mixing does not increase linearly with tidal conversion, but rather with an approximately one-third power law. Such a simple algebraic relationship between conversion and dissipation, coupled with a straightforward method to compute conversion based only on topography, stratification and barotropic tide represents a new parameterization of diapycnal mixing in stratified shelf seas, applicable at least to the broad, tidally swept NW European Shelf.

Data Availability Statement

Data presented in this manuscript are available freely and without license from the British Oceanographic Data Centre where they are stored in a repository specific to this journal article. https://www.bodc.ac.uk/resources/inventories/edmed/report/7108/1.

Acknowledgments
We thank two anonymous reviewers who offered insightful advice on our original manuscript, and which led to significant improvements in the article. Funding was received through the following projects: NERC FASTNEt: NE/I010224/1 (M. E. Inall, J. A. Mattias Green, T. P. Rippeth, M. R. Palmer), NE/I030208/1 (J. A. Mattias Green, T. P. Rippeth), NE/I030259/1 (M. R. Palmer, J. A. Polton). NERC PycnMix: NE/L003287/1 (M. E. Inall, M. Toberman), NE/L003600/1 (T. P. Rippeth, J. A. Mattias Green) NE/L003325/1 (M. R. Palmer, J. A. Polton). NERC Oceans2020 (M. E. Inall, M. R. Palmer). NERC LOIS Shelf Edge Study (M. E. Inall, T. P. Rippeth).

References

Baines, P. G. (1982). On internal tide generation models. *Deep Sea Research Part A. Oceanographic Research Papers*, *29*(3), 307–338. https://doi.org/10.1016/0198-0149(82)90098-X

Bauer, J. E., Cai, W.-J., Raymond, P. A., Bianchi, T. S., Hopkinson, C. S., & Regnier, P. A. G. (2013). The changing carbon cycle of the coastal ocean. *Nature*, *504*(7478), 61–70. https://doi.org/10.1038/nature12857

Belyaev, V. S., Gezentsvey, A. N., Monin, A. S., Ozmidov, R. V., & Paka, V. T. (1975). Spectral characteristics of small-scale fluctuations of hydrophysical fields in the upper layer of the ocean. *Journal of Physical Oceanography*, *5*(3), 492–498. https://doi.org/10.1175/1520-0485(1975)005<0492:scossf>2.0.co;2

Crawford, W. R. (1982). Pacific equatorial turbulence. *Journal of Physical Oceanography*, *12*(10), 1137–1149. https://doi.org/10.1175/1520-0485(1982)012<1137:pet>2.0.co;2

Dewey, R. K., Crawford, W. R., Gargett, A. E., & Oakey, N. S. (1987). A microstructure instrument for profiling oceanic turbulence in coastal bottom boundary layers. *Journal of Atmospheric and Oceanic Technology*, *4*(2), 288–297. https://doi.org/10.1175/1520-0426(1987)004<0288:amifpo>2.0.co;2

Doodson, T. (1921). The harmonic development of the tide-generating potential. *Proceedings of the Royal Society of London - Series A: Containing Papers of a Mathematical and Physical Character*, *100*(704), 305–329. https://doi.org/10.1098/rspa.1921.0088

Egbert, G. D., & Ray, R. D. (2001). Estimates of M 2 tidal energy dissipation from TOPEX/Poseidon altimeter data. *Journal of Geophysical Research*, *106*(C10), 22475–22502. https://doi.org/10.1029/2000jc000699

Fer, I., Müller, M., & Peterson, A. K. (2015). Tidal forcing, energetics, and mixing near the Yermak Plateau. *Ocean Science*, *11*(2), 287–304. https://doi.org/10.5194/os-11-287-2015

Fer, I., Peterson, A. K., & Ullgren, J. E. (2014). Microstructure measurements from an underwater glider in the turbulent Faroe bank channel overflow. *Journal of Atmospheric and Oceanic Technology*, *31*(5), 1128–1150. https://doi.org/10.1175/JTECH-D-13-00221.1

Garrett, C., & Munk, W. (1975). Space-time scales of internal waves: A progress report. *Journal of Geophysical Research*, *80*(3), 291–297. https://doi.org/10.1029/JC080i003p00291

Graham, J. A., O'Dea, E., Holt, J., Polton, J., Hewitt, H. T., Furner, R., et al. (2018). Amm15: A new high-resolution nemo configuration for operational simulation of the European north-west shelf. *Geoscientific Model Development*, *11*(2), 681–696. https://doi.org/10.5194/gmd-11-681-2018

Green, J. A. M., & Nycander, J. (2013). A comparison of tidal conversion parameterizations for tidal models. *Journal of Physical Oceanography*, *43*(1), 104–119. https://doi.org/10.1175/JPO-D-12-023.1

Gregg, M. C. (1980). Microstructure patches in the thermocline. *Journal of Physical Oceanography*, *10*(6), 915–943. https://doi.org/10.1175/1520-0485(1980)010<0915:mpitt>2.0.co;2

Gregg, M. C. (1989). Scaling turbulent dissipation in the thermocline. *Journal of Geophysical Research*, *94*(C7), 9686. https://doi.org/10.1029/JC094iC07p09686

Gregg, M. C., Cox, C. S., Hacker, P. W., Gregg, M. C., Cox, C. S., & Hacker, P. W. (1973). Vertical microstructure measurements in the central worth Pacific. *Journal of Physical Oceanography*, *3*(4), 458–469. https://doi.org/10.1175/1520-0485(1973)003<0458:vmmitc>2.0.co;2

Guihou, K., Polton, J., Harle, J., Wakelin, S., O'Dea, E., & Holt, J. (2018). Kilometric scale modeling of the North West European Shelf Seas: Exploring the spatial and temporal variability of internal tides. *Journal of Geophysical Research: Oceans*, *123*(1), 688–707. https://doi.org/10.1002/2017JC012960

Holt, J., & Umlauf, L. (2008). Modelling the tidal mixing fronts and seasonal stratification of the Northwest European Continental shelf. *Continental Shelf Research*, *28*(7), 887–903. https://doi.org/10.1016/j.csr.2008.01.012

Inall, M. E., Aleynik, D., Boyd, T., Palmer, M., & Sharples, J. (2011). Internal tide coherence and decay over a wide shelf sea. *Geophysical Research Letters*, *38*(23). https://doi.org/10.1029/2011GL049943

Inall, M. E., & Rippeth, T. P. (2002). Dissipation of tidal energy and associated mixing in a wide Fjord. *Environmental Fluid Mechanics*, *2*(2), 219–240. https://doi.org/10.1023/a:1019846829875

Inall, M. E., Rippeth, T. P., & Sherwin, T. J. (2000). Impact of nonlinear waves on the dissipation of internal tidal energy at a shelf break. *Journal of Geophysical Research*, *105*(C4), 8687–8705. https://doi.org/10.1029/1999JC900299

Inall, M. E., Shapiro, G., & Sherwin, T. (2001). Mass transport by non-linear internal waves on the Malin Shelf. *Continental Shelf Research*, *21*(13–14), 1449–1472. https://doi.org/10.1016/S0278-4343(01)00020-6

IOC. (1985). Manual on sea level measurement and interpretation. Volume I—Basic procedures. In *Intergovernmental Oceanographic Commission Manuals and Guides 14* (p. 83).

Jochum, M. (2009). Impact of latitudinal variations in vertical diffusivity on climate simulations. *Journal of Geophysical Research*, *114*(C1), C01010. https://doi.org/10.1029/2008JC005030

Kang, D., & Fringer, O. (2012). Energetics of barotropic and baroclinic tides in the Monterey Bay area. *Journal of Physical Oceanography*, *42*(2), 272–290. https://doi.org/10.1175/JPO-D-11-039.1

Kilcher, L. F., & Nash, J. D. (2010). Structure and dynamics of the Columbia River tidal plume front. *Journal of Geophysical Research*, *115*(C5), 1978–2012. https://doi.org/10.1029/2009JC006066

Kunze, E., Williams, A. J., & Briscoe, M. G. (1990). Observations of shear and vertical stability from a neutrally buoyant float. *Journal of Geophysical Research*, *95*(C10), 18127. https://doi.org/10.1029/JC095iC10p18127

Lincoln, B. J., Rippeth, T. P., & Simpson, J. H. (2016). Surface mixed layer deepening through wind shear alignment in a seasonally stratified shallow sea. *Journal of Geophysical Research: Oceans*, *121*(8), 6021–6034. https://doi.org/10.1002/2015JC011382

Lozovatsky, I., Lee, J.-H., Fernando, H. J. S., Kang, S. K., & Jinadasa, S. U. P. (2015). Turbulence in the East China Sea: The summertime stratification. *Journal of Geophysical Research: Oceans*, *120*(3), 1856–1871. https://doi.org/10.1002/2014JC010596

Lucas, N. S., Grant, A. L., Rippeth, T. P., Polton, J. A., Palmer, M. R., Brannigan, L., & Belcher, S. E. (2019). Evolution of oceanic near-surface stratification in response to an autumn storm. *Journal of Physical Oceanography*, *49*(11), 2961–2978. https://doi.org/10.1175/JPO-D-19-0007.1

Luneva, M. V., Wakelin, S., Holt, J. T., Inall, M. E., Kozlov, I. E., Palmer, M. R., et al. (2019). Challenging Vertical turbulence mixing schemes in a tidally energetic environment: 1. 3-D Shelf-Sea Model Assessment. *Journal of Geophysical Research: Oceans*, *124*(8), 6360–6387. https://doi.org/10.1029/2018JC014307

MacKinnon, J. A., & Gregg, M. C. (2003). Mixing on the Late-Summer New England Shelf—Solibores, shear, and stratification. *Journal of Physical Oceanography*, *33*(7), 1476–1492. https://doi.org/10.1175/1520-0485(2003)033<1476:motlne>2.0.co;2

MacKinnon, J. A., & Gregg, M. C. (2005). Near-inertial waves on the New England Shelf: The role of evolving stratification, turbulent dissipation, and bottom drag. *Journal of Physical Oceanography*, *35*(12), 2408–2424. https://doi.org/10.1175/JPO2822.1

McDougall, T., & Barker, P. (2011). *Getting started with teos-10 and the Gibbs seawater (gsw) oceanographic toolbox*. (Tech. Rep.). (p. 28). SCOR/IAPSO WG127.(ISBN: 978-0-646-55621-5).

Moum, J. N., Farmer, D. M., Smyth, W. D., Armi, L., & Vagle, S. (2003). Structure and generation of turbulence at interfaces strained by internal solitary waves propagating shoreward over the continental shelf. *Journal of Physical Oceanography*, *33*(10), 2093–2112. https://doi.org/10.1175/1520-0485(2003)033<2093:sagota>2.0.co;2

Moum, J. N., & Rippeth, T. P. (2009). Do observations adequately resolve the natural variability of oceanic turbulence? *Journal of Marine Systems*, *77*(4), 409–417. https://doi.org/10.1016/j.jmarsys.2008.10.013

Munk, W., & Wunsch, C. (1998). Abyssal recipes ii: Energetics of tidal and wind mixing. *Deep-Sea Research. Part I, Oceanographic Research Papers*, *45*(12), 1977–2010. https://doi.org/10.1016/S0967-0637(98)00070-3

Nash, J. D., Kelly, S. M., Shroyer, E. L., Moum, J. N., & Duda, T. F. (2012). The unpredictable nature of internal tides on continental shelves. *Journal of Physical Oceanography*, *42*(11), 1981–2000. https://doi.org/10.1175/JPO-D-12-028.1

Nash, J. D., Shroyer, E. L., Kelly, S. M., Inall, M. E., Duda, T. F., Levine, M. D., et al. (2012). Are Any coastal internal tides predictable? *Oceanography*, *25*(2), 80–95. https://doi.org/10.5670/oceanog.2012.44

Nycander, J. (2005). Generation of internal waves in the deep ocean by tides. *Journal of Geophysical Research*, *110*(C10), C10028. https://doi.org/10.1029/2004JC002487

Oakey, N. (1985). Statistics of mixing parameters in the upper ocean during JASIN Phase 2. *Journal of Physical Oceanography*, *15*(12), 1662–1675. https://doi.org/10.1175/1520-0485(1985)015<1662:sompit>2.0.co;2

Osborn, T. R. (1978). Measurements of energy dissipation adjacent to an island. *Journal of Geophysical Research*, *83*(C6), 2939. https://doi.org/10.1029/JC083iC06p02939

Osborn, T. R. (1980). Estimates of the local rate of vertical diffusion from dissipation measurements. *Journal of Physical Oceanography*, *10*(1), 83–89. https://doi.org/10.1175/1520-0485(1980)010<0083:eotlro>2.0.co;2

Osborn, T. R., & Crawford, W. R. (1977). *Turbulent velocity measurement with an airfoil probe* (Manuscript Report No. 31) (pp. 39–104). University of British Columbia.

Osborn, T. R., & Lueck, R. G. (1985). Turbulence measurements with a submarine. *Journal of Physical Oceanography*, *15*(11), 1502–1520. https://doi.org/10.1016/0278-4343(85)90036-610.1175/1520-0485(1985)015<1502:tmwas>2.0.co;2

Palmer, M. R., Inall, M. E., & Sharples, J. (2013). The physical oceanography of Jones Bank: A mixing hotspot in the Celtic Sea. *Progress in Oceanography*, *117*, 9–24. https://doi.org/10.1016/j.pocean.2013.06.009

Palmer, M. R., Polton, J. A., Inall, M. E., Rippeth, T. P., Green, J. A. M., Sharples, J., & Simpson, J. H. (2013). Variable behavior in pycnocline mixing over shelf seas. *Geophysical Research Letters*, *40*(1), 161–166. https://doi.org/10.1029/2012GL054638

Palmer, M. R., Rippeth, T. P., & Simpson, J. H. (2008). An investigation of internal mixing in a seasonally stratified shelf sea. *Journal of Geophysical Research*, *113*(C12), C12005. https://doi.org/10.1029/2007JC004531

Palmer, M. R., Stephenson, G. R., Inall, M. E., Balfour, C., Düsterhus, A., & Green, J. (2015). Turbulence and mixing by internal waves in the Celtic Sea determined from ocean glider microstructure measurements. *Journal of Marine Systems*, *144*, 57–69. https://doi.org/10.1016/j.jmarsys.2014.11.005

Polzin, K. L., Toole, J. M., Schmitt, R. W., & Schmitt, R. W. (1997). Estimates of diapycnal mixing in the abyssal ocean. *Science*, *264*(5162), 1120–1123. https://doi.org/10.1126/science.264.5162.1120

Prandke, H., & Stips, A. (1998). Microstructure profiler to study mixing and turbulent transport processes. In *IEEE Oceanic Engineering Society. Oceans'98. Conference Proceedings (cat. no.98ch36259)* (Vol. 1, pp. 179–183). IEEE.

Pugh, D. (1996). *Tides, surges and mean sea-level*. Jhon Wiley & Sons.

Rippeth, T. P. (2005). Mixing in seasonally stratified shelf seas: A shifting paradigm. *Philosophical Transactions. Series A, Mathematical, Physical, and Engineering Sciences*, *363*(1837), 2837–2854. https://doi.org/10.1098/rsta.2005.1662

Rippeth, T. P., Fisher, N. R., & Simpson, J. H. (2001). The cycle of turbulent dissipation in the presence of tidal straining. *Journal of Physical Oceanography*, *31*(8), 2458–2471. https://doi.org/10.1175/1520-0485(2001)031<2458:tcotdi>2.0.co;2

Rippeth, T. P., & Inall, M. E. (2002). Observations of the internal tide and associated mixing across the malin shelf. *Journal of Geophysical Research: Oceans*, *107*(C4), 31–314. https://doi.org/10.1029/2000JC000761

Rippeth, T. P., Palmer, M. R., Simpson, J. H., Fisher, N. R., & Sharples, J. (2005). Thermocline mixing in summer stratified continental shelf seas. *Geophysical Research Letters*, *32*(5), L05602. https://doi.org/10.1029/2004GL022104

Rippeth, T. P., Simpson, J. H., Williams, E., & Inall, M. E. (2003). Measurement of the rates of production and dissipation of turbulent kinetic energy in an energetic tidal flow: Red wharf bay revisited. *Journal of Physical Oceanography*, *33*(9), 1889–1901. https://doi.org/10.1175/1520-0485(2003)033<1889:motrop>2.0.co;2

Schultze, L. K. P., Merckelbach, L. M., & Carpenter, J. R. (2017). Turbulence and mixing in a shallow shelf sea from underwater gliders. *Journal of Geophysical Research: Oceans*, *122*(11), 9092–9109. https://doi.org/10.1002/2017JC012872

Sharples, J., Mayor, D. J., Poulton, A. J., Rees, A. P., & Robinson, C. (2019). Shelf sea biogeochemistry: Nutrient and carbon cycling in a temperate shelf sea water column. *Progress in Oceanography*, *177*, 102182. https://doi.org/10.1016/j.pocean.2019.102182

Sharples, J., Tweddle, J. F., Mattias Green, J., Palmer, M. R., Kim, Y.-N., Hickman, A. E., et al. (2007). Spring-neap modulation of internal tide mixing and vertical nitrate fluxes at a shelf edge in summer. *Limnology & Oceanography*, *52*(5), 1735–1747. https://doi.org/10.4319/lo.2007.52.5.1735

Sherwin, T. J. (1988). Analysis of an internal tide observed on the Malin Shelf, North of Ireland. *Journal of Physical Oceanography*, *18*(7), 1035–1050. https://doi.org/10.1175/1520-0485(1988)018<1035:aoaito>2.0.co;2

Simpson, J. H., Crawford, W. R., Rippeth, T. P., Campbell, A. R., & Cheok, J. V. S. (1996). The Vertical structure of turbulent dissipation in shelf seas. *Journal of Physical Oceanography*, *26*(8), 1579–1590. https://doi.org/10.1175/1520-0485(1996)026<1579:tvsotd>2.0.co;2

Simpson, J. H., & Hunter, J. R. (1974). Fronts in the Irish Sea. *Nature*, *250*(5465), 404–406. https://doi.org/10.1038/250404a0

Simpson, J. H., & Tinker, J. P. (2009). A test of the influence of tidal stream polarity on the structure of turbulent dissipation. *Continental Shelf Research*, *29*(1), 320–332. https://doi.org/10.1016/j.csr.2007.05.013

Stephenson, G., Hopkins, J. E., Green, J. A. M., Inall, M. E., & Palmer, M. R. (2015). Baroclinic energy flux at the continental shelf edge modified by wind-mixing. *Geophysical Research Letters*, *42*(6), 1826–1833. https://doi.org/10.1002/2014GL062627

St. Laurent, L., & Simmons, H. (2006). Estimates of power consumed by mixing in the ocean interior. *Journal of Climate*, *19*(19), 4877–4890. https://doi.org/10.1175/JCLI3887.1

Thorpe, S. A., Green, J. A. M., Simpson, J. H., Osborn, T. R., & Smith, W. (2008). Boils and turbulence in a weakly stratified shallow tidal sea. *Journal of Physical Oceanography*, *38*(8), 1711–1730. https://doi.org/10.1175/2008JPO3931.1

Thorpe, S. A., & Liu, Z. (2009). Marginal instability? *Journal of Physical Oceanography*, *39*(9), 2373–2381. https://doi.org/10.1175/2009JPO4153.1

Tonani, M., Sykes, P., King, R. R., McConnell, N., Péquignet, A.-C., O'Dea, E., et al. (2019). The impact of a new high-resolution ocean model on the Met Office North-West European Shelf forecasting system. *Ocean Science*, *15*(4), 1133–1158. https://doi.org/10.5194/os-15-1133-2019

van Haren, H., Maas, L., Zimmerman, J. T. F., Ridderinkhof, H., & Malschaert, H. (1999). Strong inertial currents and marginal internal wave stability in the central North Sea. *Geophysical Research Letters*, *26*(19), 2993–2996. https://doi.org/10.1029/1999GL002352

Vic, C., Naveira Garabato, A. C., Green, J. A. M., Spingys, C., Forryan, A., Zhao, Z., & Sharples, J. (2018). The lifecycle of semidiurnal internal tides over the Northern Mid-Atlantic Ridge. *Journal of Physical Oceanography*, *48*(1), 61–80. https://doi.org/10.1175/JPO-D-17-0121.1

Vic, C., Naveira Garabato, A. C., Green, J. A. M., Waterhouse, A. F., Zhao, Z., Melet, A., et al. (2019). Deep-ocean mixing driven by small-scale internal tides. *Nature Communications*, *10*(1), 2099. https://doi.org/10.1038/s41467-019-10149-5

Washburn, L., & Gibson, C. H. (1984). Horizontal variability of temperature microstructure at the base of a mixed layer during MILE. *Journal of Geophysical Research*, *89*(C3), 3507. https://doi.org/10.1029/JC089iC03p03507

Waterhouse, A. F., MacKinnon, J. A., Nash, J. D., Alford, M. H., Kunze, E., Simmons, H. L., et al. (2014). Global patterns of diapycnal mixing from measurements of the turbulent dissipation rate. *Journal of Physical Oceanography*, *44*(7), 1854–1872. https://doi.org/10.1175/JPO-D-13-0104.1

Zaron, E. D., & Egbert, G. D. (2006). Estimating open-ocean barotropic tidal dissipation: The Hawaiian Ridge. *Journal of Physical Oceanography*, *36*(6), 1019–1035. https://doi.org/10.1175/JPO2878.1